



Article

# Strap-On Magnets: A Framework for Rapid Prototyping of Magnets and Beam Lines

Volker Ziemann

Department of Physics and Astronomy, FREIA, Uppsala University, 75120 Uppsala, Sweden; volker.ziemann@physics.uu.se

**Abstract:** We describe a framework to assemble permanent-magnet cubes in 3D-printed frames to construct dipole, quadrupole, and solenoid magnets, whose field, in the absence of iron, can be calculated analytically in three spatial dimensions. Rotating closely spaced dipoles and quadrupoles in opposite directions allows us to adjust the integrated strength of a multipole. The contributions of unwanted harmonics were calculated and found to be moderate. We then combined multiple magnets to construct beam-line modules: a chicane, a triplet cell, and a solenoid focusing system.

**Keywords:** permanent magnet; magnet prototyping; dipole magnet; quadrupole magnet; solenoid magnet



**Citation:** Ziemann, V. Strap-On Magnets: A Framework for Rapid Prototyping of Magnets and Beam Lines. *Instruments* **2021**, *5*, 36. <https://doi.org/10.3390/instruments5040036>

Academic Editor: Antonio Ereditato

Received: 11 November 2021

Accepted: 29 November 2021

Published: 1 December 2021

**Publisher's Note:** MDPI stays neutral with regard to jurisdictional claims in published maps and institutional affiliations.



**Copyright:** © 2021 by the author. Licensee MDPI, Basel, Switzerland. This article is an open access article distributed under the terms and conditions of the Creative Commons Attribution (CC BY) license (<https://creativecommons.org/licenses/by/4.0/>).

## 1. Introduction

Various types of magnets play important roles in many physics laboratories. Unfortunately, they are often expensive and require long lead times to order. Here we propose a complementary method: we constructed multipole magnets from standard-size permanent-magnet cubes, which are reasonably inexpensive and easy to obtain. Moreover, we suggest to hold them in 3D-printed frames or CNC-machined aluminum frames that can be produced in most small workshops. By constructing the frames in two halves, they can be wrapped-around or strapped-on to circular pipes and easily fixed with non-magnetic screws, which makes retrofitting them to existing beam lines very simple. Figure 1 illustrates the frames for a dipole and a quadrupole constructed from eight cubes, each.

The orientation of the cubes in the frames follows the Halbach method [1], adapted to square [2] instead of trapezoidal magnet segments. In an  $M$ -magnet dipole, subsequent magnets along the azimuth are rotated by  $2 \times 360^\circ / M$ . The left-hand image in Figure 1 illustrates this for a dipole made of eight cubes. In the frame for an eight-magnet quadrupole, shown on the right-hand image in Figure 1, subsequent magnets rotate by  $3 \times 360^\circ / 8$  as illustrated by the little notch in each of the eight holes for the cubes.

In order to calculate the magnetic fields from the cubes in three dimensions, we used the closed-form expressions from [3], which allowed us to prepare MATLAB [4] scripts to determine the relevant field quantities and the multipole contents of the magnets in parameterized form. This proves very convenient to adapt the design to different sized cubes, different geometries, and other multipolarities.

The organization of this report is as follows: after we discuss the design of the frames with the OpenSCAD [5] software, we characterize eight-magnet dipoles, quadrupoles, and solenoids made of 10 mm cubes. Then, we combine two dipoles or quadrupoles to produce dipoles and quadrupoles whose field strength can be varied, where we follow an approach that is complementary to those discussed in [1,6,7]. In order to illustrate the use of the variable multipoles, we combined several such magnets to beam-line modules, which was inspired by the early permanent-magnet based anti-proton recycler ring at Fermilab [8] and, more recently, by CBETA [9].

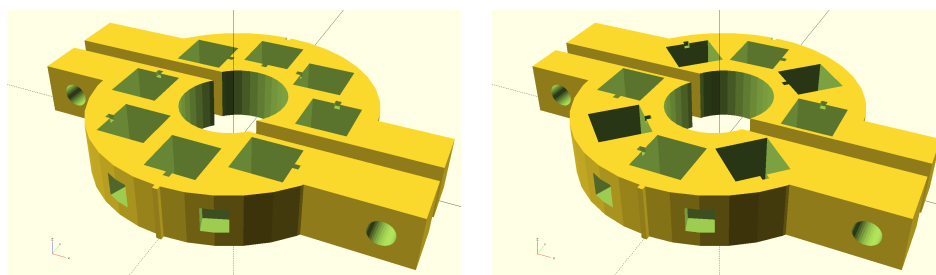


**Figure 1.** The frames for dipoles (left) and quadrupoles (right).

## 2. Frames

We used OpenSCAD to prepare solid models of the frames to hold the permanent-magnet cubes, because this CAD software is easily scriptable, such that parameters for different-sized magnets of multipoles only require changing a few parameters. The frame can then be exported in a format that is compatible with 3D printers or CNC milling machines, which allows for short prototyping cycles.

The frame consists of a cylinder with an outer radius of  $r_o = 28$  mm, a 1 mm notch and a groove on its outer periphery to tell up from down, and 5 mm square holes to later attach handling rods. Furthermore, there are rectangular solids to later hold screws—the horizontal circular holes shown in Figure 1. Moreover, a circular hole with a radius of  $r_i = 10$  mm was removed from the center. The holes for the 10 mm cubes were then “stamped out” from this base frame. Each of the holes is born at the center, receives the little notch, and is rotated by an angle  $m\phi$ , where  $m$  is the multipolarity of the magnets and  $\phi$  is the azimuthal position of the cube in the frame. Then, it is moved outwards by  $o = 18$  mm along the  $x$ -axis before being rotated once again by  $\phi$ , which puts the hole in place. We point out that the notches on the holes are only for orientation; in the magnets, we used that direction to indicate the “feather” (and not the “tip”) of the arrows that indicate the easy axis of the magnets. Typically, the square holes for the cubes are 0.1 mm larger than the magnet cubes themselves, which makes inserting the cubes easier. Inside the holes, they are then easily fixated with super-glue.

Note that these frames have semi-circular holes with a diameter of  $2r_i = 20$  mm in their center. Again, in order to account for finite tolerances of the frame and the pipe, normally the diameter needs to be increased a little, say, by 0.1 mm. This makes it easy to wrap the frames around a circular pipe, align the holes for the screws, and insert the screws and tighten them. This fixes the frame in place. Moving it along the pipe or rotating it only involves loosening the screws, moving the frame with the magnets, and tightening the screws again.

Let us now investigate the properties of the magnetic field generated by cubes in such a frame—first out are dipoles.

## 3. Dipole

In [3], we calculated the field generated by a rectangular current sheet, which proved useful to describe permanent-magnet cubes that can be modeled by four rectangular sheets. In the top-left image in Figure 2, we see that each of the eight magnets consists of four blue sheets with the green line indicating the direction of the current, such that we can visualize the cube as a square solenoid that generates a magnetic field in its inside that is represented by the yellow arrow, which coincides with the direction of the easy axis of the magnet. In all our simulations, we assumed the remanent field of all cubes to be  $B_r = 1.47$  T. Inside the ring-shaped assembly with the eight cubes, we see red arrows indicating the direction of the field in the mid-plane. The vertical field  $B_y$  along the dotted black line is shown on the top-right plot, which shows a magnitude of about 0.24 T with a curved dependence in the  $x$ -direction, indicating some higher multipole components. The plot on the bottom-right shows  $B_y$  along a line in the  $z$ -direction. We observed that the fringe fields roll off slowly and extend far beyond the  $\pm 5$  mm physical size of the

magnets. Finally, we determined the multipoles of the assembly by integrating the field in the range  $|z| < 40$  mm along lines perpendicular to the cyan circle, which had a radius of 5 mm. We then Fourier-transformed the component of the field that is tangential to this circle and showed it on the upper panel on the bottom-left in Figure 2. This algorithm, which is explained in [3], gives us the magnitude and angle of the multipole coefficients of the assembly shown on the middle panel. We see that the integrated field strength was 5.72 Tmm, and the lower panel indicates that the relative magnitude of the other multipoles was around  $6 \times 10^{-3}$  with the decapole contribution ( $m = 5$ ) being the largest.

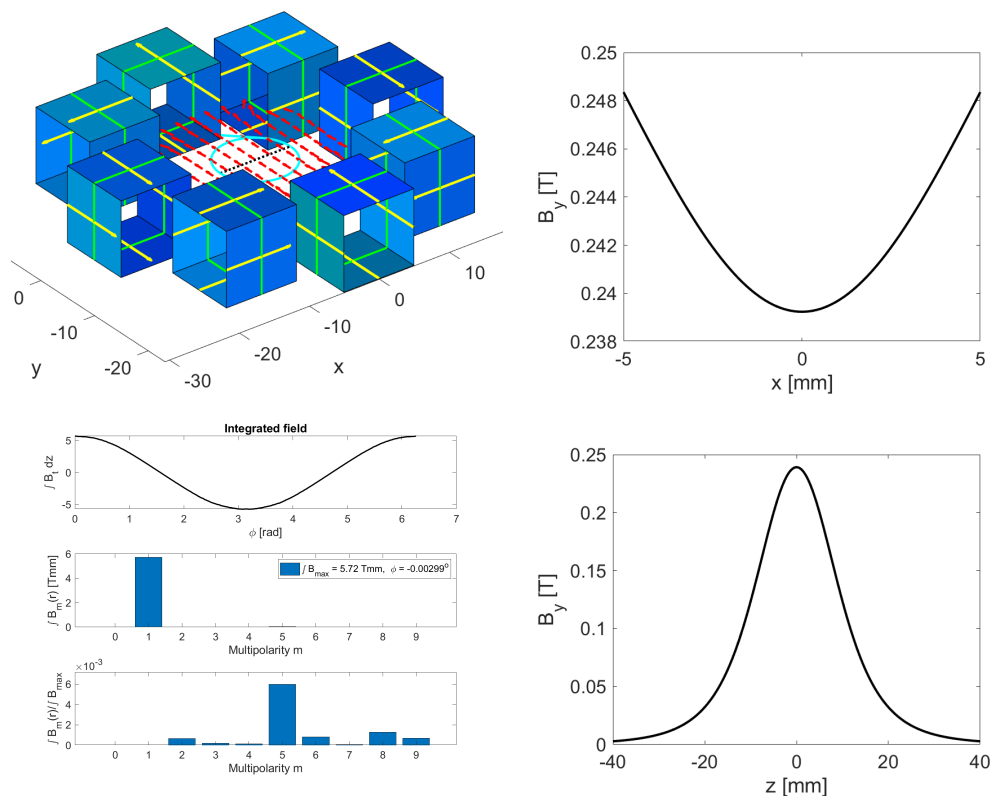


**Figure 2.** Top left: the eight cubes for a dipole are shown as hollow blue cubes and the magnetic field by red arrows. Top right: the vertical field  $B_y$  along the black dotted line shown on the top-left image. Bottom right:  $B_y$  along the axis perpendicular through the center of the ring. Bottom left: the tangential field on the cyan circle (upper panel); the dominant field harmonic, here for a dipole (middle); and the relative strength for the unwanted multipoles (bottom).

We conclude that the eight-cube dipole magnet reached a peak field of 0.24 T and had an integrated field strength of 5.72 Tmm, while the relative magnitude of unwanted multipoles on a circle with a 5 mm radius was below  $6 \times 10^{-3}$ .

#### 4. Quadrupole

The field of the quadrupole assembly corresponding to the frame from the right in Figure 1 is shown in Figure 3. The top-left image shows the eight cubes with the red arrows indicating the field in the mid-plane, the black dotted line, and the cyan circle on which the multipoles were calculated. The top-right plot shows  $B_y$  along the black dotted line and indicates a linearly rising field along the  $x$ -axis that is characteristic for a quadrupole. From the slope, we determined a gradient in the mid-plane of 32.7 T/m. The gradient along the  $z$ -axis in the middle of the assembly is visible on the bottom-right plot. We observed that even the fringe fields of the quadrupole extended beyond its physical size of  $\pm 5$  mm but decayed faster than those of a dipole. The image with the three panels on the bottom-left shows the tangential field component around the azimuth, which clearly

displays two oscillations, indicating a quadrupolar field. This was also verified on the middle panel, which showed an integrated field 3.13 Tmm, which, when dividing by the 5 mm radius of the circle, resulted in an integrated gradient of 0.63 T. The lower panel shows that all other multipoles contributed less than  $4 \times 10^{-3}$  in magnitude.

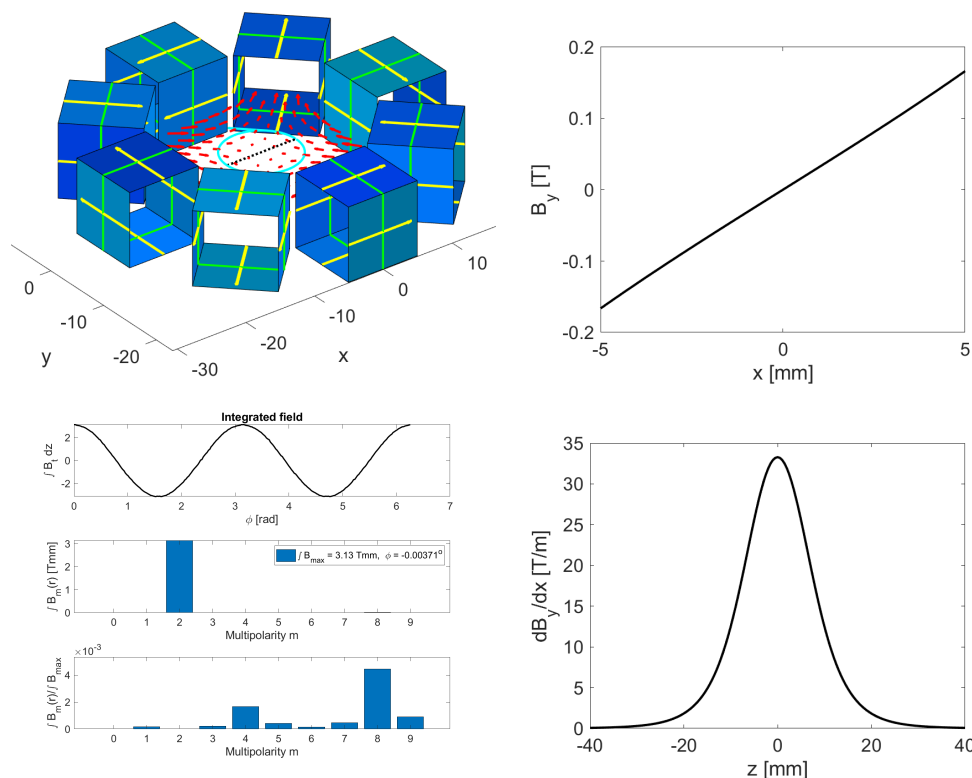


**Figure 3.** Top left: the eight cubes for a quadrupole are shown as hollow blue cubes and the magnetic field by red arrows. Top right: the vertical field  $B_y$  along the black dotted line shown on the top-left image. Bottom right: the gradient  $dB_y/dx$  along the axis perpendicular through the center of the ring. Bottom left: the tangential field on the cyan circle (upper panel), the dominant field harmonic, here for a quadrupole (middle); and the relative strength for the unwanted multipoles (bottom).

### 5. Solenoids

It turns out that the frame for the quadrupoles can also be used to construct both axial and radial solenoids; for an axial solenoid, we only have to insert all cubes with their easy axis pointing along the  $z$ -axis. The top-left image in Figure 4 illustrates this. Note also the black dotted line and the cyan circle in the midplane as well as the solid magenta line to illustrate the  $z$ -axis. The top-right plot shows the  $z$ -component  $B_z$  of the magnetic field in the midplane along the black dotted line visible on the top-left image. We see that it has a parabolic shape—the magnitude of the field closer to the permanent magnets is higher. We see that  $B_z$  points opposite the direction of the easy axis of the cubes and reached about  $-0.16$  T in the center of the assembly. On the lower-right plot, we also observed that  $B_z$ , after being negative in the center of the assembly, became positive with a magnitude of 0.03 T around  $z = \pm 20$  mm. On the three-panel image on the bottom-left, we explored the impact of approximating the solenoid by eight cubes. The upper panel shows  $B_z$  in the midplane of the assembly around the cyan circle, which had a radius of 5 mm. We observed eight oscillations as we moved around the azimuth  $\phi$ , whose amplitude, however, was rather small—less than  $10^{-4}$  times the magnitude of the average  $B_z$ , which was 0.185 T at  $r = 5$  mm. We conclude that, even though the field quality is limited, constructing solenoids is feasible within our framework.

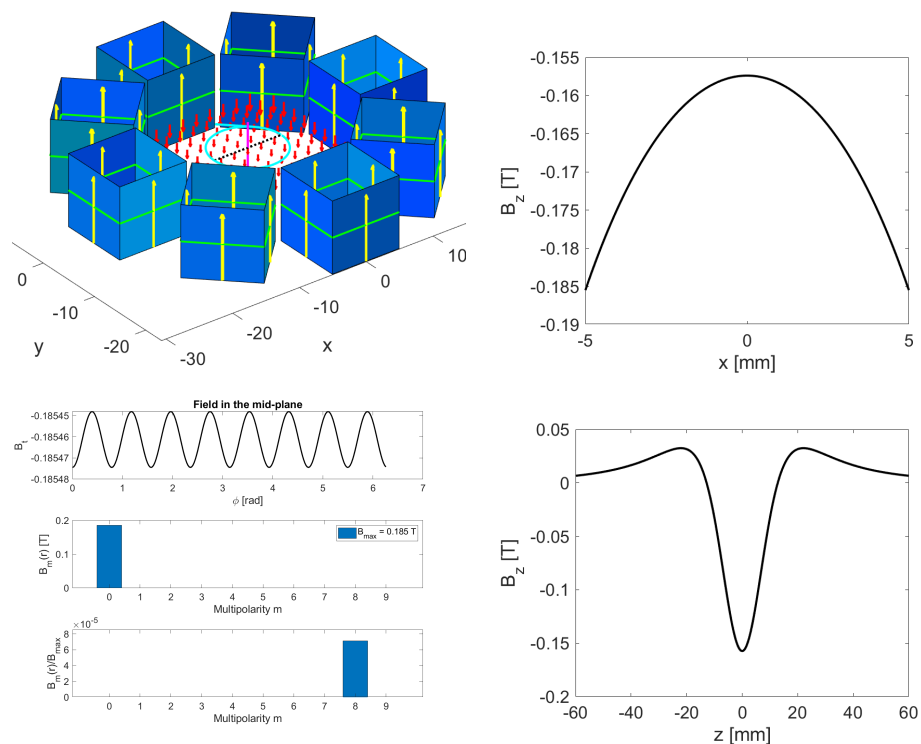


**Figure 4.** Top left: the eight cubes for an axial solenoid are shown as hollow blue cubes and the magnetic field by red arrows. Top right: the axial field  $B_z$  along the black dotted line shown on the top-left image. Bottom right:  $B_z$  along the axis perpendicular through the center of the ring. Bottom left: the axial field  $B_z$  on the cyan circle (upper panel), the dominant field harmonic, here constant (middle); and the relative strength for the unwanted harmonics.

Likewise we can construct a radial solenoid by rotating the cubes such that their easy axis either points inwards or outwards, and we can construct one solenoid from two rings, separated by 20 mm, as shown in Figure 5. The easy axes of the left eight-cube rings point inward, and those of the right ring point outward. The magnetic field is illustrated by the red arrows and points from the right towards the left assembly along the negative  $z$ -axis in the intermediate region. The plot on the right-hand side in Figure 5 shows  $B_z$  along the  $z$ -axis, where  $z = 0$  corresponds halfway between the two assemblies whose position is indicated by the blue dashed boxes. We see that the maximum value exceeded 0.2 T in the center and reached about 0.12 T just outside the two assemblies. The homogeneity of the field was comparable to that of the axial solenoid close to the cubes and was better in the intermediate region.

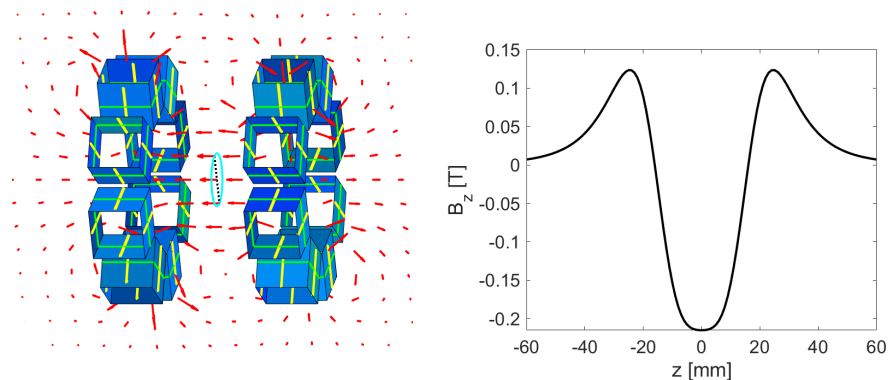


**Figure 5.** Left: a radial solenoid made of two rings and the field illustrated by the red arrows. Right: the axial field  $B_z$  along a line through the center of the two rings.

### 6. Adjustable Dipole

Inspired by the observation that the fields of two very short magnets with opposite polarity almost cancel and the fact that the fringe fields of the dipole from Section 3 extend far beyond the physical length of the magnet, we placed two dipole rings very close to each other (2 mm between the rings) and then rotated one with respect to the other. The images on the left-hand side in the top and middle row of Figure 6 illustrate the geometry of these assemblies. On the top left, the two eight-cube rings were aligned, and the one below the upper ring was rotated by  $\psi = 30^\circ$  counter-clockwise, while the lower ring was rotated by  $30^\circ$  clockwise.

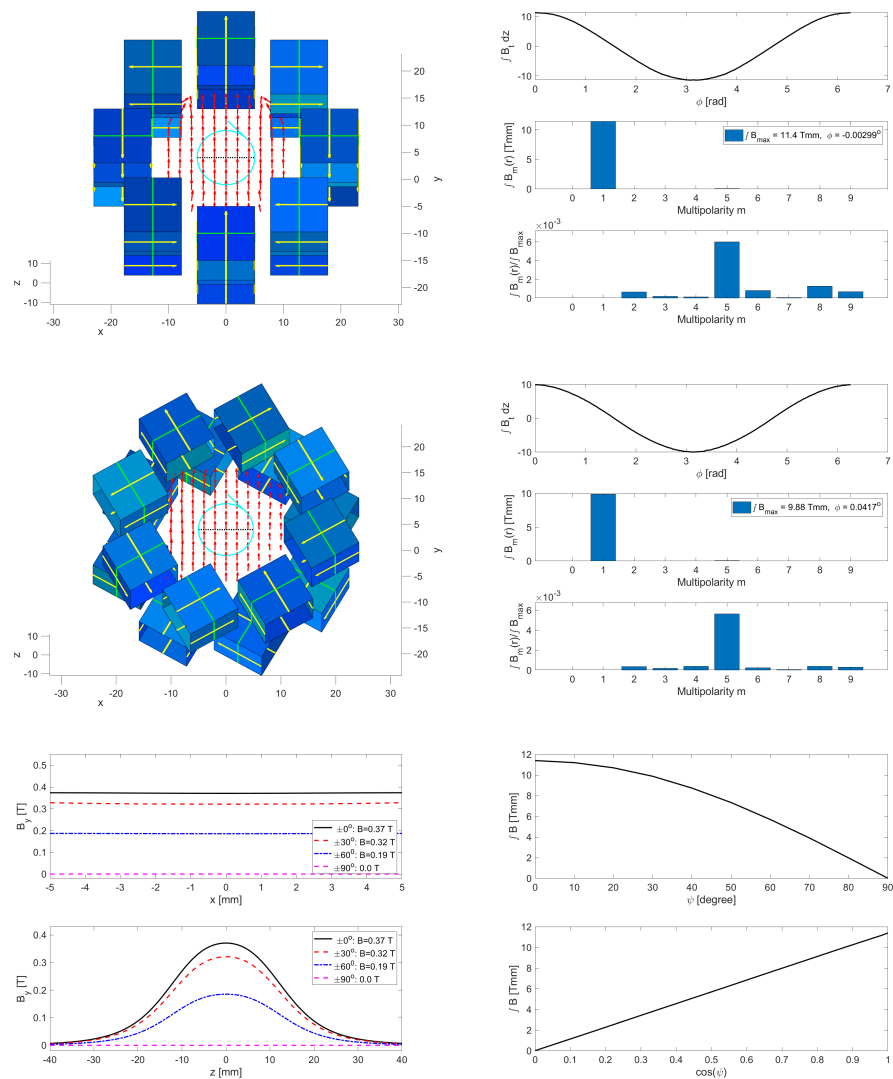


**Figure 6.** Top left: two rings for a variable dipole aligned on top of each other. Top right: the tangential field on the cyan circle (upper), the dominant field harmonic (middle), and the relative strength of the unwanted harmonics (bottom). Middle row: the corresponding images for rings rotated with  $\psi = 30^\circ$ . The integrated strength was reduced, but the unwanted harmonics were similar to the plot above. Bottom left: the fields along the black dotted line for different rotation angles  $\psi$  (upper) and  $B_y$  along a line through the center of the two rings. Bottom right: the integrated field plotted versus  $\psi$  (upper) and  $\cos \psi$  (lower).

The three-panel images towards the right of the respective geometries illustrate the integrated multipole content of the assemblies. In the upper panel on the top-right image, we see that the tangential field component of the field integral showed a sinusoidal

pattern that was responsible for the dominant dipole component visible on the middle panel. The integrated strength of 11.4 Tmm of this assembly was twice that of the single magnet from Figure 2, because the fields superimpose linearly in ideal permanent-magnet assemblies. Furthermore, the lower panel shows that the dominant higher multipole was the decapole ( $m = 5$ ) component whose contribution was  $6 \times 10^{-3}$  smaller than the main component. The right-hand image in the middle row shows the integrated field of the assembly with the two rotated magnets. The tangential field shown on the upper panel was also sinusoidal, albeit with a reduced amplitude of 9.88 Tmm, which is also given in the legend of the middle panel with the Fourier-harmonics. Even in the rotated geometry, the dipole contribution was dominant, and the relative contributions of the unwanted harmonics, shown on the lower panel, were below  $6 \times 10^{-3}$ .

That the dominant effect of rotating two eight-cube magnets with opposite angles  $\psi$  only changed the integrated field from 11.4 to 9.88 Tmm but did not adversely affect the unwanted multipoles encouraged us to explore the dependence of the field integral for different rotation angles  $\psi$ . The image on the left-hand side in the bottom row shows the vertical field  $B_y$  along the  $z$ -axis on the lower panel for  $\psi = 0^\circ, 30^\circ, 60^\circ$ , and  $90^\circ$ . We see that rotating the two eight-cube rings reduces the peak field in the center of the magnet from 0.37 T down to zero. The upper panel shows  $B_y$  on the  $x$ -axis along the black dotted line, and we see that the field was rather constant—only the amplitude was different for different values of  $\psi$ . The lower panel shows the fringe fields of  $B_y$  along  $z$  for the four values of  $\psi$ .

Finally, we systematically varied  $\psi$  in steps of  $10^\circ$  and showed the integrated field component (or the amplitude of the Fourier harmonic for  $m = 1$ ) as a function of  $\psi$  on the upper panel in the image on the right-hand side in the bottom row of Figure 6. We observed that the integrated field decrease in a smooth curve from 11.4 Tmm down to zero at  $\psi = 90^\circ$ , where the easy axes of cubes on top of each other have opposite polarities and cancel one another. On the lower panel, we show the same data but plot versus  $\cos \psi$  instead. We found that now the integrated field strength shows a linear dependence on  $\cos \psi$ , which indicates that the integrated field is given by twice the integrated field of one eight-cube ring times  $\cos \psi$ . However, this is just the projection of the maximum field of the rings onto the vertical axis. The field components along the vertical axis add, but along the horizontal axis they cancel. This will make tuning and setting up of such double-dipole assemblies rather straightforward.

## 7. Adjustable Quadrupole

It is certainly no surprise that the same idea also works with quadrupoles. On the top-left image is Figure 7, in which we show the geometry of two aligned ( $\psi = 0$ ) eight-cube quadrupoles on top of each other with a 2 mm space between the rings. On the image on the middle row below, we show the same assembly, but the upper ring is rotated by  $\psi = 20^\circ$  and the lower ring by  $-20^\circ$ . The images towards the right of the geometries show the tangential field on the upper panel, the Fourier harmonics on the middle panel, and the relative magnitude of the unwanted harmonics on the bottom panel. We observed that the dominant harmonic was the quadrupolar  $m = 2$  with integrated strength, evaluated at a radius of 5 mm, going from 6.26 Tmm for  $\psi = 0^\circ$  to 4.79 Tmm for  $\psi = 20^\circ$ . The harmonics in all cases were smaller by a few times  $10^{-3}$ .

Next, we systematically changed  $\psi$  in steps of  $5^\circ$  from  $0^\circ$  to  $45^\circ$  and showed the gradient on the mid-plane (indicated by the black dotted line) on the lower-left image in Figure 7. We see that the gradient changed from 45.8 T/m for  $\psi = 0^\circ$  to zero at  $\psi = 45^\circ$ . On the right-hand image on the bottom row, we plotted the integrated gradient  $\int (dB_y/dx) dz$  as a function of  $\psi$  in the upper panel. We see that it moves smoothly from 6.26 Tmm/5 mm = 1.25 T for  $\psi = 0^\circ$  to zero at  $\psi = 45^\circ$ . On the bottom panel, we plotted the same data versus  $\cos 2\psi$  and found a linear dependence of the integrated gradient on  $\cos 2\psi$ , which will make tuning and setting up double-quadrupole assemblies straightforward.

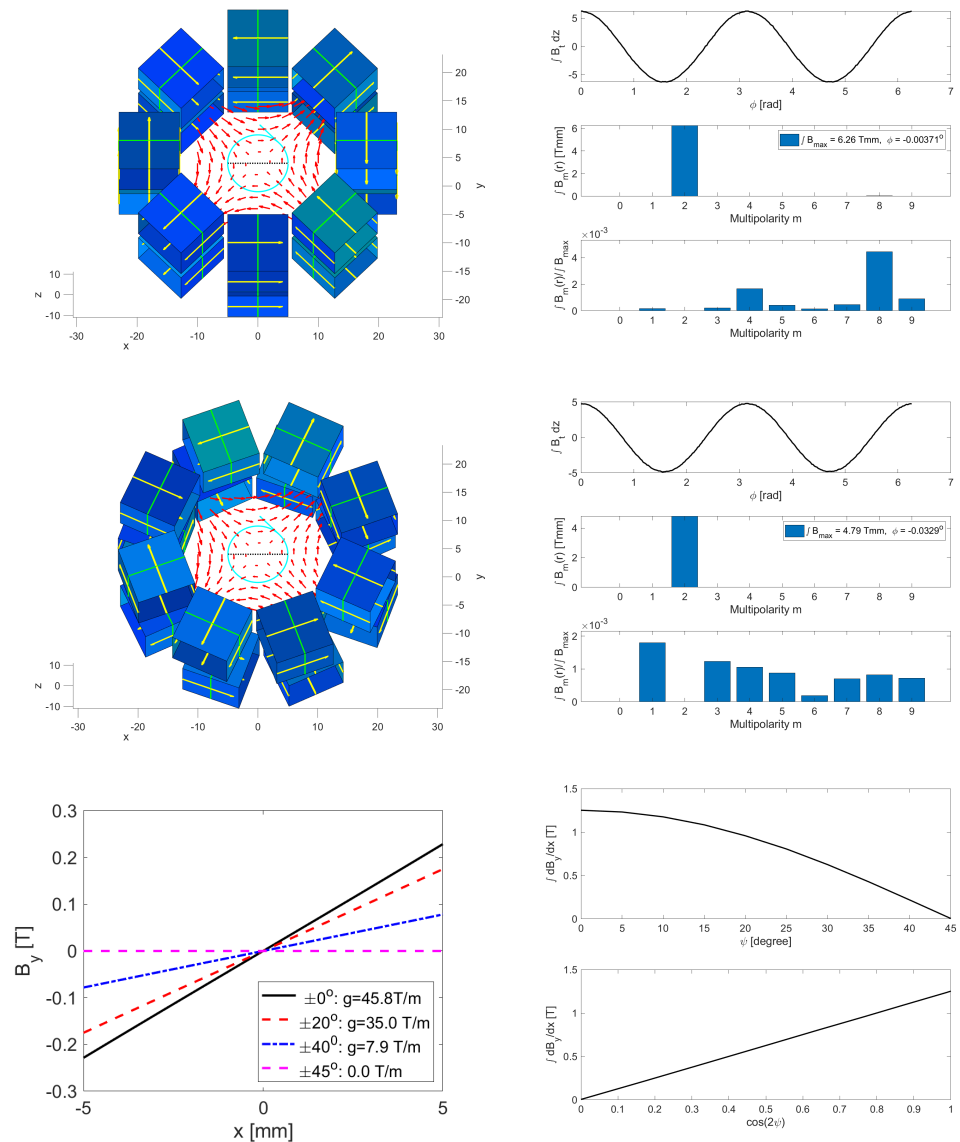


**Figure 7.** Top left: two rings for a variable quadrupole aligned on top of each other. Top right: the tangential field on the cyan circle (upper), the dominant field harmonic (middle), and the relative strength of the unwanted harmonics (bottom). Middle row: the corresponding images for rings rotated with  $\psi = 20^\circ$ . The amplitude was reduced, but the unwanted harmonics were similar to the plot above. Bottom left: the gradient along the black dotted line for different rotation angles  $\psi$ . Bottom right: the integrated gradient as a function of the rotation angle  $\psi$  (upper) and as a function of  $\cos 2\psi$ .

### 8. Some Applications

Here we discuss three examples where the strap-on magnets might prove useful: a small chicane, a triplet cell, and a solenoid lens. Let us start with the chicane.

#### 8.1. Chicane

Four-dipole chicanes are frequently used in accelerators to provide an energy-dependent path length for a beam, which helps to compress beams longitudinally [2,10]. The figure of merit for a bunch compressor is the  $R_{56} \approx -2L\phi^2$ , where  $L$  is the distance between the outer and the inner two dipoles, and  $\phi$  is the deflection angle of one dipole. This angle is given by the ratio of the integrated field  $\int B_y dz$  of the dipole and the momentum of the beam, often expressed through its rigidity  $B\rho$ . For a beam with momentum 300 MeV/c, the rigidity is

about 1 Tm, such that the variable two-magnet dipole from Section 6 with an integrated field of 11.4 Tmm deflects a 300 MeV beam by 11.4 mrad. With  $L = 0.4$  m between the dipoles, we therefore deflected the beam by about 5 mm and stayed within the region shown on the bottom left in Figure 6. Furthermore, we found  $R_{56} = -0.10$  mm. Since we can adjust the magnetic field by rotating the two adjacent dipoles, we can adjust the  $R_{56}$  between the maximum value and zero.

Figure 8 illustrates such a chicane with four variable dipoles wrapped around the grey beam pipe. One of the magnets was colored light blue and had a handle attached sticking out to the top right, while the other magnet was colored yellow and had a handle sticking out towards the top left. The handles were attached to the 5 mm square holes on the periphery of the frames, which is also visible on Figure 1. Moreover, careful inspection shows that the two middle assemblies have opposite polarity (the central ones have a notch sticking out at the top, while the outer ones have a groove), such that they deflect a beam in opposite directions. Connecting all yellow handles with a rod allows to change the rotation angle of all yellow magnets by the same amount, while a rod connecting the light blue handles rotates all light blue magnets by the same amount, which permits to change the excitation of all dipoles synchronously. Small variations in the excitation of different magnets can be compensated by placing small plates between the handles and the connecting rod. Note that for the illustration in Figure 8 the distance  $L$  was reduced to 0.2 m.

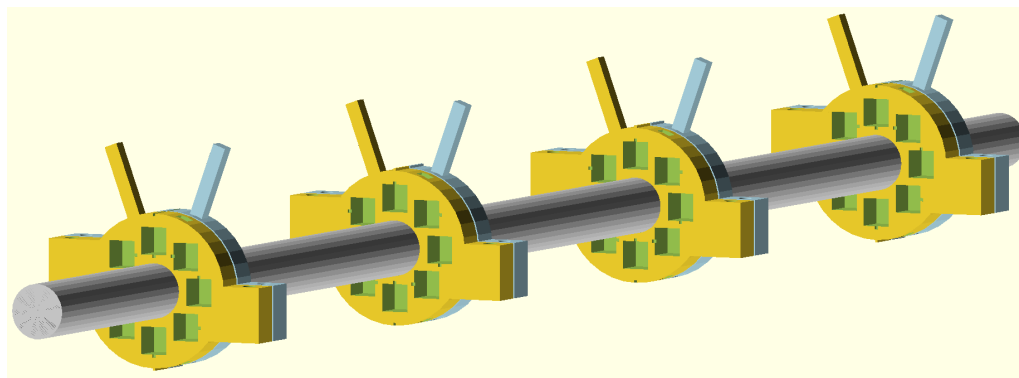


**Figure 8.** Sketch of the four-dipole chicane made of four double-ring variable dipole magnets strapped on a cylindrical pipe.

### 8.2. Triplet Cell

In beam lines where long stretches of free space between magnets as well as round beams are required, often triplets are used. They are combinations of three closely spaced quadrupoles where the first and third quadrupole are excited equally, and the center quadrupole has opposite polarity and twice the excitation. Figure 9 shows the magnet lattice with the three thin-lens quadrupoles and the horizontal beta function  $\beta_x$  in the upper panel and the vertical beta function  $\beta_y$  in the lower panel. The black lines show the beta functions for the thin lens model with a betatron phase advance per cell of  $60^\circ$  in both planes. Note that the magnets are only located over a distance of 0.6 m such that there is almost 4 m free space available between magnets of adjacent cells.

Our quadrupole rings are particularly attractive to realize such triplets; we used a single ring for the two outer quadrupoles and two rings, rotated by  $90^\circ$ , for the double-strength center quadrupole with opposite polarity. The lower image in Figure 10 shows the two outer rings located near  $z = \pm 300$  mm and the inner double-ring near  $z = 0$  mm. The magenta line denotes the axis on which beam travels. We point out that adjusting the relative rotation angle  $\psi$  between the two center quadrupoles gives us some tunability. The upper image in Figure 10 shows the gradient along the beam axis. Note the opposite polarity of the outer and inner quadrupoles. Moreover, the black line shows the field for  $\psi = 0^\circ$  and the red line for  $\psi = 20^\circ$ .

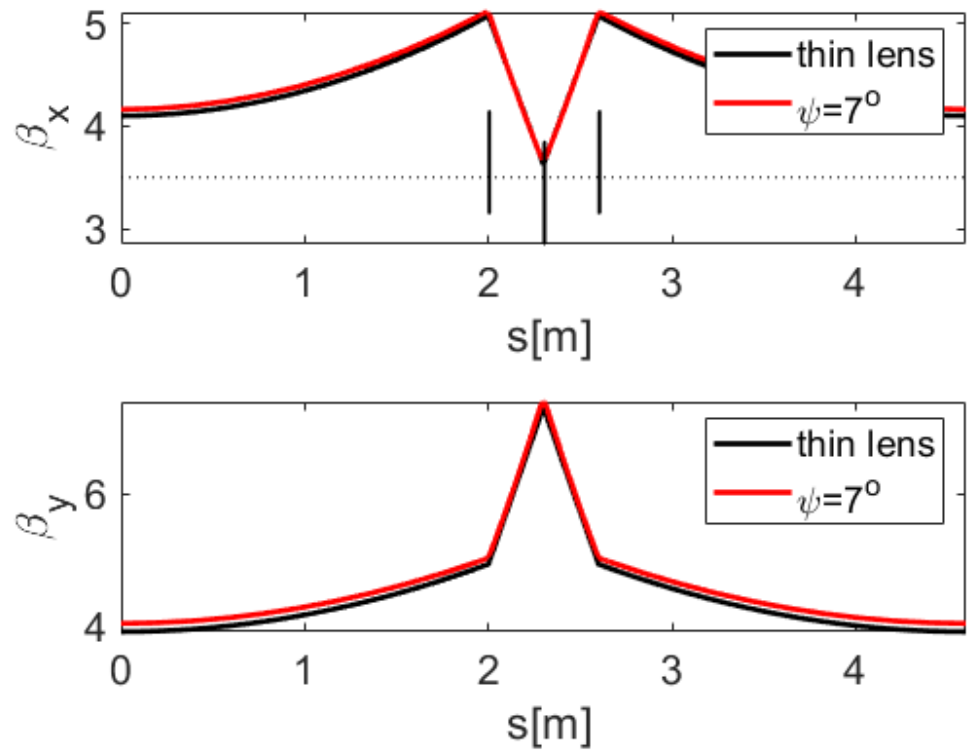


**Figure 9.** The horizontal (top) and vertical (bottom) beta functions of a cell made of thin-lens quadrupoles (black lines) with  $60^\circ$  phase advance in both planes. The red lines are the corresponding beta functions where the fields of quadrupole rings from Figure 10 were used, and the central double-ring quadrupole was rotated by  $\psi = 7^\circ$ .

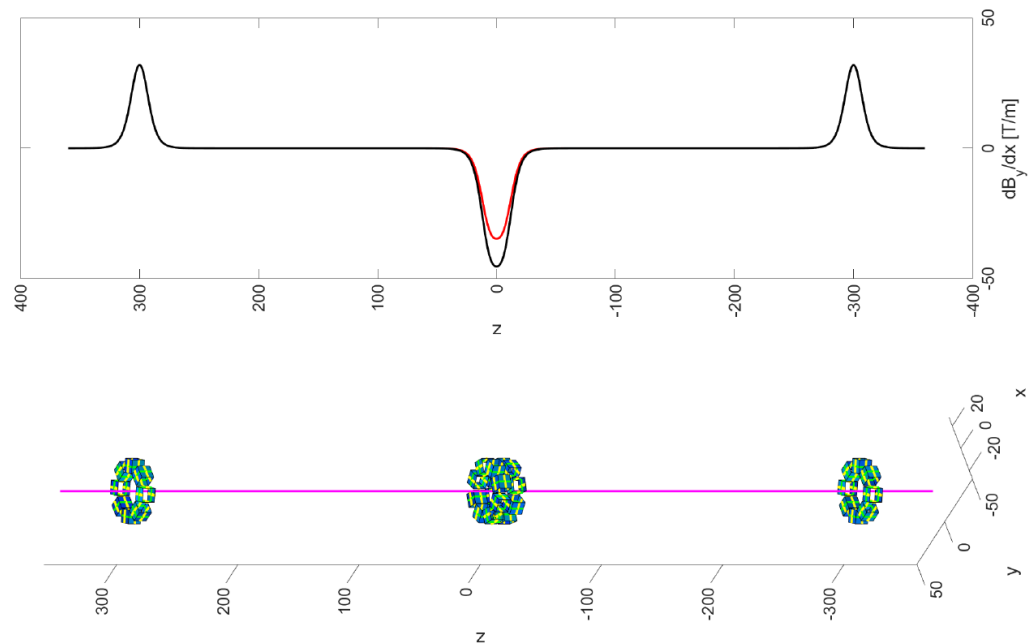


**Figure 10.** Bottom: four quadrupole rings assembled to form a triplet. The strength of the double-ring is adjustable as described in Section 7. Top: the gradient along the beam line for rotation angles of the central quadrupoles of  $\psi = 0^\circ$  (black) and  $\psi = 20^\circ$  (red).

We then empirically adjusted  $\psi$ ; calculated the gradient along the beam axis; automatically wrote a beam-line description, consisting of many 1 mm long quadrupoles; and

calculated the beta function with software from [2]. With  $\psi = 7^\circ$ , we found that the phase advances were close to the  $60^\circ$  for the thin-lens lattice. The red lines in Figure 9 showed  $\beta_x$  and  $\beta_y$  for the gradients produced by our quadrupole rings, which agreed very well with those of the thin-lens model, shown in black.

### 8.3. Solenoid Focusing

The radial solenoid from Section 5, whose geometry and field are shown in Figure 5, is suitable to focus round low-energy beams. In the upper panel of Figure 11, we show the beam envelope of a 5 MeV electron beam with a normalized emittance of  $\epsilon_n = 10^{-6}$  m rad passing through two such radial solenoids spaced 1.75 m apart. On the lower panel, we recognize  $B_z$  from the right-hand image in Figure 5—once near  $z = 0$  and once near  $z = 1.75$  m. The envelope was calculated from  $B_z$  by numerically integrating the paraxial-ray equation [11]. The initial beam was parallel and had a radius of 1 mm but then developed a focus near  $z = 0.87$  m, which is consistent with the focal length  $f$  calculated from  $1/f = \int B_z^2 dz / (2B\rho)^2 \approx 0.87$  m, where we had  $\int B_z^2 dz = 1.3 \times 10^{-3} \text{ T}^2\text{m}$  and  $B\rho = 0.0169 \text{ Tm}$  for the 5 MeV beam.

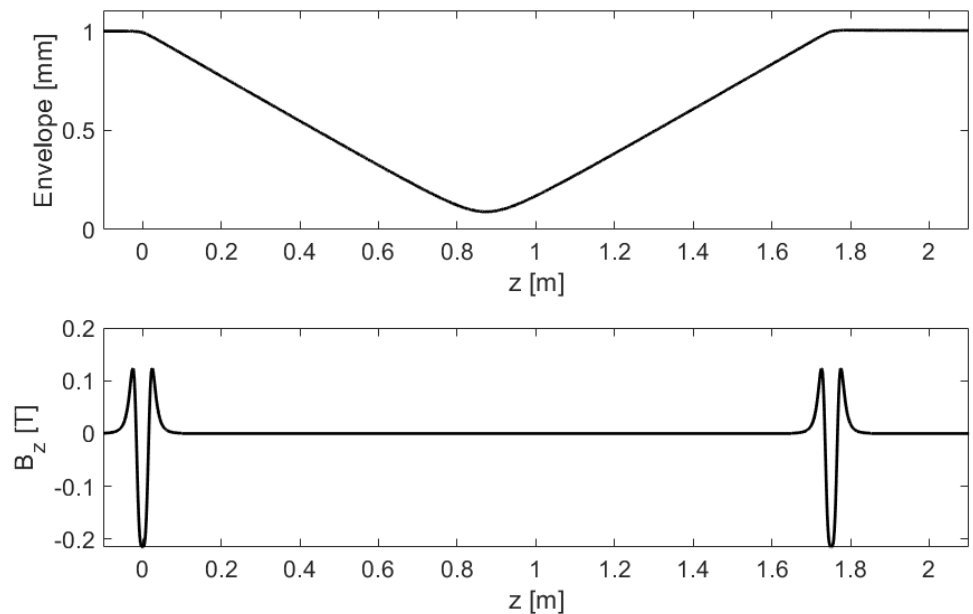


**Figure 11.** The longitudinal field  $B_z$  created by two radial solenoids located at  $z = 0$  and  $z = 1.75$  m (bottom) and the beam envelope of a 5 MeV electron beam with a parallel beam with radius 1 mm entering from the left (top). We see that the first solenoid focused the beam to a waist near  $z = 0.87$  m, and the second one makes the beam parallel again.

Making the solenoid stronger is a simple matter of repeating multiple copies of the radial solenoids, as shown in Figure 12, where six copies of the solenoid from Figure 5 follow with equal distance between consecutive rings. Note that the polarity alternates from one ring to the next. The upper panel shows the beam axis in magenta together with the twelve radial solenoids with alternating polarity, whereas the lower panel shows the longitudinal component  $B_z$  on the beam axis. Note that the rings are placed every 30 mm, and the amplitude of  $B_z$  reaches  $\pm 0.2$  T. The integrated focusing strength  $\int B_z^2 dz$  was  $8.8 \times 10^{-3} \text{ T}^2\text{m}$  for this configuration. This configuration would work for a 13 MeV electron beam ( $B\rho \approx 0.044 \text{ Tm}$ ) where it leads to a comparable focal length close to 0.9 m.

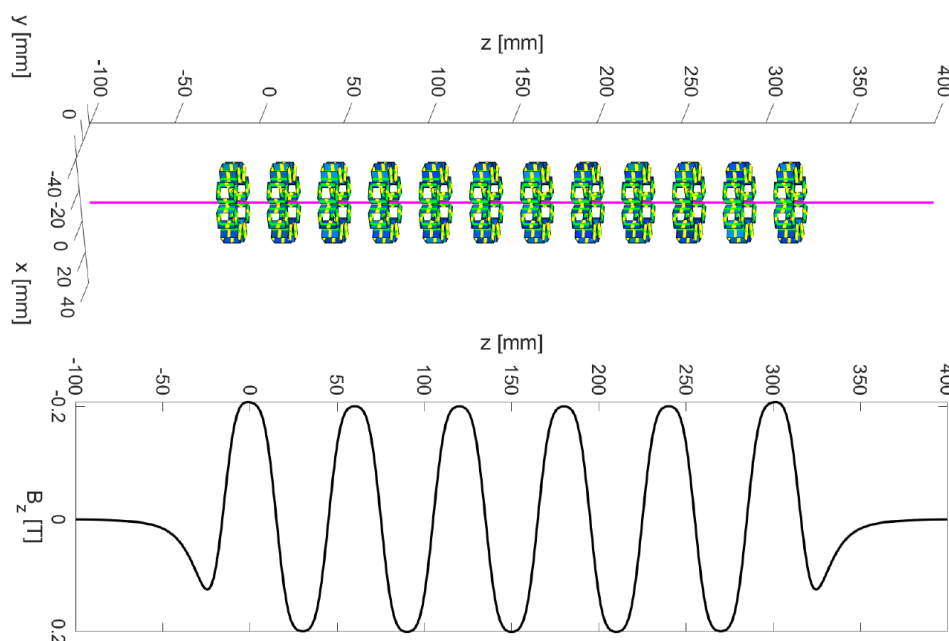


**Figure 12.** Assembling the six two-ring radial solenoids with alternating polarity, shown in the upper panel, created the longitudinal field  $B_z$  shown in the lower panel. It has a larger focusing strength than the two-ring solenoid used in Figure 11 and can be used for higher-energy beams.

## 9. Scaling

We point out that changing the value of the remanent magnetic field  $B_r$  will just scale the field values reported in the remainder of this report accordingly.

Moreover, changing the linear dimensions, the size of cubes  $w$ , their radial position  $o$ , and the size of the frame, will keep all quantities, whose dimension is Tesla, unchanged. For example, the field in a dipole made of 5 mm cubes equals that of a dipole made of 10 mm cubes, but its fringe field does not extend as far as that of the bigger dipole. Therefore the integrated field of the smaller magnet is a factor of two smaller. Likewise, the integrated gradient of a quadrupole made of 5 mm cubes is the same as that made of 10 mm cubes. In the smaller magnet, the gradient is doubled, but the total length is halved.

## 10. Conclusions

Based on the analytic results for the magnetic fields from permanent magnets from [3], we explored the use of permanent-magnet cubes to create dipoles, quadrupoles, and solenoids. All examples were based on the frames for 10 mm cubes, shown in Figure 1, but are easily scalable to use cubes of a different size, to include more cubes or to produce other multipoles. We found that the magnets have reasonably good field qualities; the amplitudes of the harmonics at a radius of 5 mm in all cases were less than a fraction of a percent and often better.

An attractive feature is the possibility to retrofit these magnets to existing beam lines without having to open the vacuum system; the two magnet halves are simply strapped-on to the beam pipe. A second attractive feature is the possibility to combine two closely spaced rings to obtain dipoles and quadrupoles whose strength is continuously adjustable, while their field quality is comparable to that of a single ring.

Finally, we found these magnet rings suitable to construct beam-line modules for chicanes, a triplet cell, and solenoids focusing a low-energy beam.

**Funding:** In part, funding was provided through the project *Disseminating technology for cold magnets to provide access to a wider international market*, which is supported by the European Regional Development Fund (ERDF) and Region Kronoberg.

**Institutional Review Board Statement:** Not applicable.

**Informed Consent Statement:** Not applicable.

**Data Availability Statement:** Matlab scripts used to generate the images are available from <https://github.com/volkziem/PermanentMagnetDesign>.

**Conflicts of Interest:** The author declares no conflict of interest.

## References

1. Halbach, K. Design of Permanent Multipole Magnets with Oriented Rare Earth Cobalt Magnets. *Nucl. Instrum. Methods* **1980**, *169*, 1–10. [[CrossRef](#)]
2. Ziemann, V. *Hands-On Accelerator Physics Using MATLAB*; CRC Press: Boca Raton, FL, USA, 2019.
3. Ziemann, V. Closed-form expressions for the magnetic field of permanent magnets in three dimensions. *arXiv* **2021**, arXiv:2106.04153.
4. Mathworks Web Page. Available online: <https://www.mathworks.com/> (accessed on 28 November 2021).
5. OpenSCAD Project Web Page. Available online: <https://openscad.org/> (accessed on 28 November 2021).
6. Halbach, K. Conceptual Design of a Permanent Quadrupole Magnet with Adjustable Strength. *Nucl. Instrum. Methods* **1983**, *206*, 353. [[CrossRef](#)]
7. Gluckstern, R.; Holsinger, R. Variable strength focussing with permanent magnet quadrupoles. *Nucl. Instrum. Methods* **1981**, *187*, 119. [[CrossRef](#)]
8. Jackson, G. (Ed.) *Fermilab Recycler Ring Technical Design Report*; FERMILAB-TM-1981; Fermi National Accelerator Laboratory: Batavia, IL, USA, 1996.
9. Hoffstaetter, G.H.; Trbojevic, D.; Mayes, C.; Banerjee, N.; Barley, J.; Bazarov, I.; Bartnik, A.; Berg, J.S.; Brooks, S.; Burke, D.; et al., CBETA Design Report, Cornell-BNL ERL Test Accelerator. *arXiv* **2017**, arXiv:1706.04245.
10. Stulle, F.; Adelman, A.; Pedrozzi, M. Designing a bunch compressor chicane for a multi-TeV linear collider. *Phys. Rev. Spec.-Top.-Accel. Beams* **2007**, *10*, 031001. [[CrossRef](#)]
11. Reiser, M. *Theory and Design of Charged Particle Beams*; Wiley-VCH: Weinheim, Germany, 2004.